



Subject Areas:

xxxxx, xxxxx, xxxxx

Keywords:

xxxx, xxxx, xxxx

Author for correspondence:

F. Shi

e-mail: f.shi12@imperial.ac.uk

The validity of Kirchhoff theory for scattering of elastic waves from rough surfaces

F. Shi⁽¹⁾, W. Choi⁽²⁾, M. J. S. Lowe⁽¹⁾, E. A. Skelton⁽³⁾ and R. V. Craster⁽³⁾

⁽¹⁾ Department of Mechanical Engineering, Imperial College London, SW7 2AZ, United Kingdom

⁽²⁾ Center for Safety Measurement, KRISS, 267 Gajeong-Ro Yuseong-Gu Daejeon 305-340, Rep. of Korea

⁽³⁾ Department of Mathematics, Imperial College London, SW7 2AZ, United Kingdom

The Kirchhoff approximation (KA) for elastic wave scattering from 2D and 3D rough surfaces is critically examined using finite element (FE) simulations capable of extracting highly accurate data whilst retaining a fine-scale rough surface. The FE approach efficiently couples a time domain finite element solver with a boundary integration method to compute the scattered signals from specific realizations of rough surfaces. Multiple random rough surfaces whose profiles have Gaussian statistics are studied by both Kirchhoff and FE models and the results are compared; Monte Carlo simulations are used to assess the comparison statistically. The comparison focuses on the averaged peak amplitude of the scattered signals, as it is an important characteristic measured in experiments.

Comparisons, in both 2D and 3D, determine the accuracy of Kirchhoff theory in terms of an empirically estimated parameter σ^2/λ_0 (σ is the root mean square value, and λ_0 is the correlation length, of the roughness), being considered accurate when this is less than some upper bound c , ($\sigma^2/\lambda_0 < c$). The incidence and scattering angles also play important roles in the validity of the Kirchhoff theory and it is found that for modest incidence angles of less than 30° the accuracy of the Kirchhoff approximation is improved even when $\sigma^2/\lambda_0 > c$. In addition, the evaluation results are compared using 3D isotropic rough surfaces and 2D surfaces with the same surface parameters.

1. INTRODUCTION

The Kirchhoff approximation (KA) is the classical methodology often used to calculate the scattering behavior from rough surfaces. It is widely used in many fields, such as underwater acoustics [1], radar detection [2], and seismology [3,4], to produce fast predictions of statistics for the scattering of waves via a Monte Carlo approach. For elastic media there is strong interest in Nondestructive Evaluation (NDE) and ultrasonics in applying the Kirchhoff model to understand the scattering behavior from rough defects as this is of critical importance in assessing the structural integrity of, for instance, components in the nuclear industry. In that area early work by Ogilvy [5] studied the effects of roughness on scattered wave amplitude-based and time-based sizing techniques, and concluded that careful interpretation of measured data is required when roughness is present. More recently, Zhang et al. [6] have investigated the effect of roughness and inclined angles on sizing the defect using the ultrasonic array imaging with the total focusing method (TFM). Given the wide ranging use of Kirchhoff theory to estimate defect size it is natural to want to constrain, or determine, the range of this uncertainty; this is just one example amongst many where clarity over the KA range of validity is required.

It is well known, as pointed out by Ogilvy [7], that Kirchhoff theory is a high frequency approximation and its accuracy depends on many factors (surface roughness, grazing incidence/scattering angles, etc.). It is therefore important to find the range of validity, and when the use of KA should be expected to be reliable, particularly as it is used for safety critical inspection. Historically there have been several attempts to evaluate the accuracy of KA, and Ogilvy provided a detailed summary in her book [7]. For instance, in [8], Ogilvy implemented a variational principle to quantify the accuracy of the scalar KA. Another evaluation was provided by Thorsos [1] comparing the boundary integration method and acoustic Kirchhoff theory using random Gaussian surfaces. The conclusion was that the correlation length λ_0 is the most critical parameter and the root mean square (RMS) σ also affects the accuracy of the Kirchhoff model. A similar study was extended to a Pierson-Moskowitz sea surface [9] and the KA was shown to accurately predict the incoherent scattering near the specular direction for incident grazing angles as low as 10° ; this is typical of the impressive accuracy and utility that has led to the widespread use of Kirchhoff theory.

The above examples are all for scalar problems, and the validity of the vector wave KA (occurring in electromagnetics and elastodynamics) differs from the scalar case. The difference is because restrictions on surface properties that arise from effects such as shadowing and multiple scattering can be made more severe by mode conversion, into bulk waves and surface, or interfacial, waves. Chen and Fung [10] investigated electromagnetic wave scattering from rough surfaces by the KA and the moment method finding that electromagnetic Kirchhoff theory provides good agreement over small angles of incidence when $k\sigma$ is less than 0.2 and $k\lambda_0$ is less than or equal to 2.0. Here k is the incident wavenumber. Robertsson et al. [3] compared the elastic KA with the finite difference method (FDM) and the spectral element method (SEM) with an application in reflection seismology. In this work, some discrepancies between the KA and the other two methods were shown particularly in terms of amplitudes. Elastic Kirchhoff theory was also investigated in connection with the application in NDE by Roberts [11], who compared it with the boundary element (BE) method. More recently, Zhang et al. [12] calculated the scattering matrix from Gaussian rough defects in comparison with the finite element method and concluded that the elastic KA is valid with the roughness $\sigma \leq 0.3\lambda$ and $\lambda_0 \geq 0.5\lambda$ at incidence and scattering angles over the range from -80° to 80° .

However, to the best knowledge of the authors, all of these previous research papers regarding the range of validity of the Kirchhoff theory, especially in the elastodynamic regime, are only based on 2D rough surfaces or at most 2.5D (corrugated) surfaces due to limitations in the simulation methods used. We are now in a position to sidestep these limitations and perform highly accurate numerical simulations in 3D due to recent advances such as hybrid methods [13,14]. We have been motivated to explore the validity of Kirchhoff theory in 3D

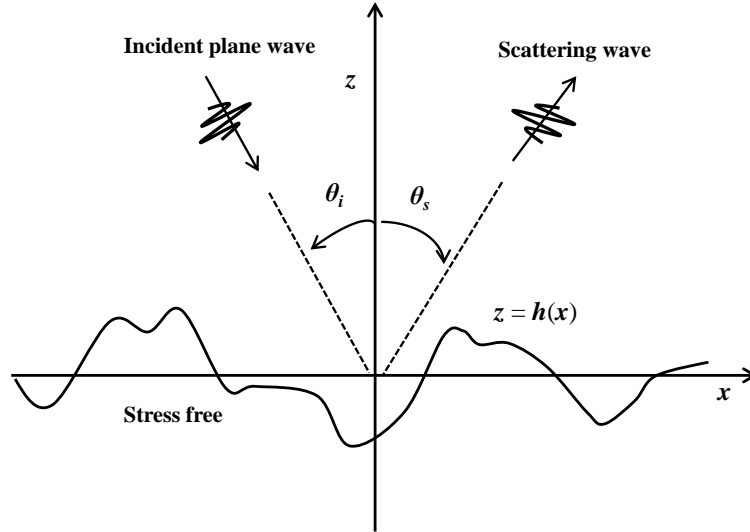


Figure 1. Sketch of the scattering geometry: Plane wave in an elastic material incident on an infinitely long surface with stress-free boundary condition.

as researchers developing modelling tools using 3D KA for NDE in the power industry have observed significant differences of several dB between experimentally measured reflections from rough defects and KA simulations of the same cases [15]. These discrepancies arise because surface scattering in a real inspection is an inherently complex process, involving phenomena such as mode conversions, surface waves and shadowing, which are not at all included in the Kirchhoff approximation. These phenomena are known to cause the greatest errors when the angle of incidence and the height of the roughness are large, and are also expected to be different for 2D and 3D. Therefore, to gain a comprehensive understanding of the performance of the 3D Kirchhoff theory on random rough surfaces, with height variations in both x and y directions, it is necessary to actually simulate the full 3D problems. Motivated by the experimental observations, and the apparent discrepancies with the KA in elasticity, we carefully examine the range of validity of both the 3D and 2D elastic KA by comparison to a reference numerical method. Using an empirical procedure the ratio σ^2/λ_0 is found to be important in determining the region of validity of the KA, and this ratio has different upper bounds in 2D and 3D. In addition the incident angle also affects the performance of the KA.

This paper is organized as follows: Section 2 introduces the numerical models, including the rough surface profile, the Kirchhoff model and the finite element boundary integration method used as a reference for comparison. Section 3 describes details of the simulations in both 2D and 3D. Error analysis in 2D and 3D is discussed in Section 4, and the concluding remarks are made in Section 5.

2. NUMERICAL MODELS

We intend to simulate, as closely as possible, the scattering of a plane wave from an infinite rough surface and the scattering geometry (in 2D) is depicted in Fig. (1). The incident and scattering angles are denoted as θ_i and θ_s , respectively, and a stress-free boundary condition is assumed along the rough surface.

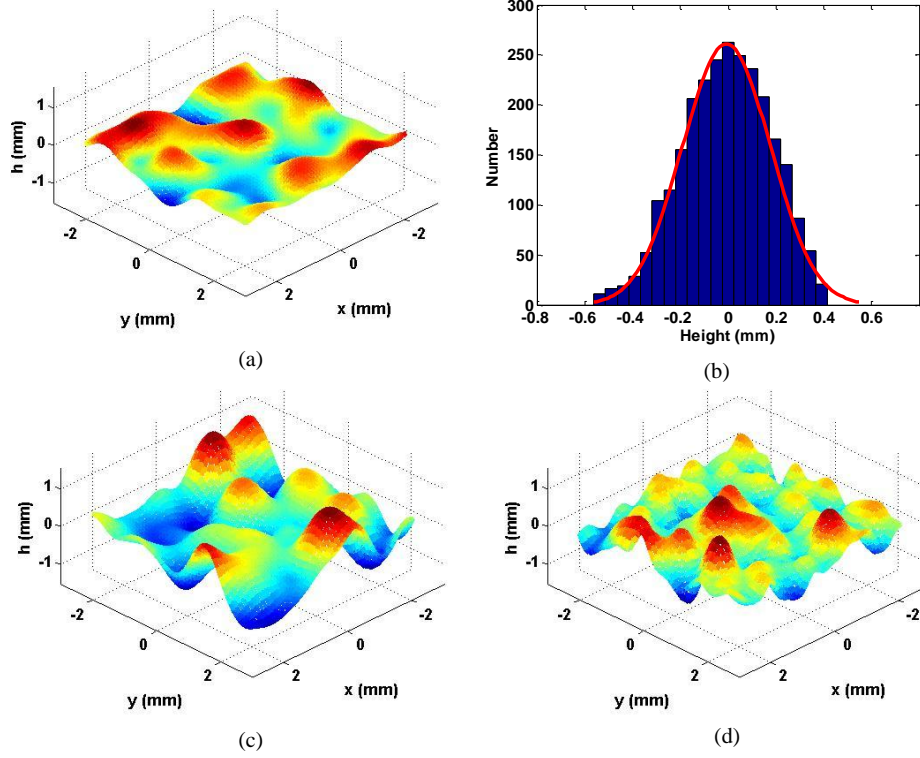


Figure 2. 3D isotropic Gaussian rough surface profiles. (a) $\sigma = \lambda_p/6$, $\lambda_0 = \lambda_p/2$. (b) Height distribution of the surface shown in (a) and the corresponding Gaussian fit curve. (c) $\sigma = \lambda_p/3$, $\lambda_0 = \lambda_p/2$. (d) $\sigma = \lambda_p/6$, $\lambda_0 = \lambda_p/4$.

(a) Gaussian random rough surface

The surface of the defect is represented as 'rough' in the sense that the surface height data obeys a certain statistical distribution, and these realistic surface profiles are generated using some statistical parameters. Gaussian random surfaces were commonly used historically [1,16], and also some fatigue cracks are found experimentally to have a Gaussian spectrum [12]. Therefore we use Gaussian surfaces herein to find the region of validity of KA. Fig. (2) shows a typical 3D isotropic (the roughness varies in the same manner in both x and y directions) Gaussian rough surface profile, with the mean value of height data $h(x, y)$ being zero. The probability density function $p(h)$ is used to describe the statistical distribution of the height data, which is a Gaussian function in this study:

$$p(h) = \frac{1}{\sigma\sqrt{2\pi}} \exp\left(-\frac{h^2(x, y)}{2\sigma^2}\right) \quad (2.1)$$

σ is the RMS of height and the empirical formula to estimate σ is then given by:

$$\sigma = \sqrt{\langle h^2 \rangle} = \sqrt{\frac{1}{N} \sum_{i=1}^N h_i^2}. \quad (2.2)$$

The RMS value determines the height scale of the surface. In addition, the lateral variation of surface height is described by the correlation function which for a Gaussian surface is

$$C(\mathbf{R}) = \frac{\langle h(\mathbf{r})h(\mathbf{r} + \mathbf{R}) \rangle}{\sigma^2} = \exp \left[- \left(\frac{x^2}{\lambda_x^2} + \frac{y^2}{\lambda_y^2} \right) \right]. \quad (2.3)$$

In (2.3) λ_x and λ_y are called the correlation lengths in the x and y directions, as distances over which the correlation function falls by $1/e$; we assume an isotropic rough surface hereafter, implying $\lambda_x = \lambda_y = \lambda_0$. In this isotropic case the correlation function simplifies to:

$$C(R) = \exp \left(- \frac{R^2}{\lambda_0^2} \right) \quad (2.4)$$

with $R^2 = x^2 + y^2$.

The commonly used moving average method [16] is utilized to generate the rough surface by controlling the RMS value σ and the correlation length λ_0 . They are in units relative to the compressional wavelength λ_p . This method first produces a series of uncorrelated random numbers that are convolved with a set of weighting functions to calculate the required surface height data $h(x, y)$. Fig. (2)(a) and (b) show one realization of a 3D Gaussian rough surface and the corresponding height distribution function. The effect of changing σ and λ_0 on the roughness is clearly seen in Fig. (2)(c) and (d), compared with the original surface profile in Fig.(2)(a). It should be noted that each generated realization of the surface profile is not identical given the random nature of the surface. However, for a specific σ and λ_0 , all realizations should follow the same statistical parameters and can be classified into the same category. In later sections Monte Carlo simulations are run for different categories of rough surfaces, and a general rule with respect to the statistical parameters regarding the validity of the KA is obtained.

(b) Finite element boundary integration approach

The finite element method is a very general numerical tool that is highly effective for elastic wave problems, and we use it as a reference against which to evaluate the accuracy of the Kirchhoff theory. However, full 3D FE modelling is very computationally expensive and even the 3D free meshing of the irregular surface depends on the irregularity of the defect shape. To overcome these issues, that have limited previous studies to 2D or 2.5D simulations, we use a state-of-the-art finite element boundary integration method implemented in a GPU-driven software package Pogo [17], with a mixed meshing algorithm in 3D. This package is sophisticated in its use of computer hardware, algorithms and in utilising hybrid methods. Efficient and accurate Monte Carlo simulations using the FE method in 3D are performed; for brevity the full details of the methodology are not included here as they are given in [13].

The FE model to calculate the scattering from a rough surface when internal waves are incident, is shown in Fig. (3). A rough backwall is surrounded by smooth surfaces extended into an absorbing region [18]. The smooth transition between the rough part and the smooth part is achieved by multiplying a spatial Hanning window to the whole bottom surface. A plane P wave is excited by forcing along a line located just above the rough backwall. Specific time traces of forces, which are calculated from a finite difference time domain method (FDTD) using a modified forcing approach [19], are fed into each excitation node. This approach was initially designed to calculate forcing signals to excite the correct incident waves inside a rectangular box. Here we simply use the code to obtain the forces on one side of the box, denoted as the excitation line. It should be noted here that the two tips of the excitation line need to be buried into the absorbing region to prevent any unwanted circular-crested waves, which would otherwise be generated from the two ends.

After executing the FE computation in the local box, the boundary displacements recorded at the rough surface are used in the Helmholtz integration with a stress-free boundary condition [20]

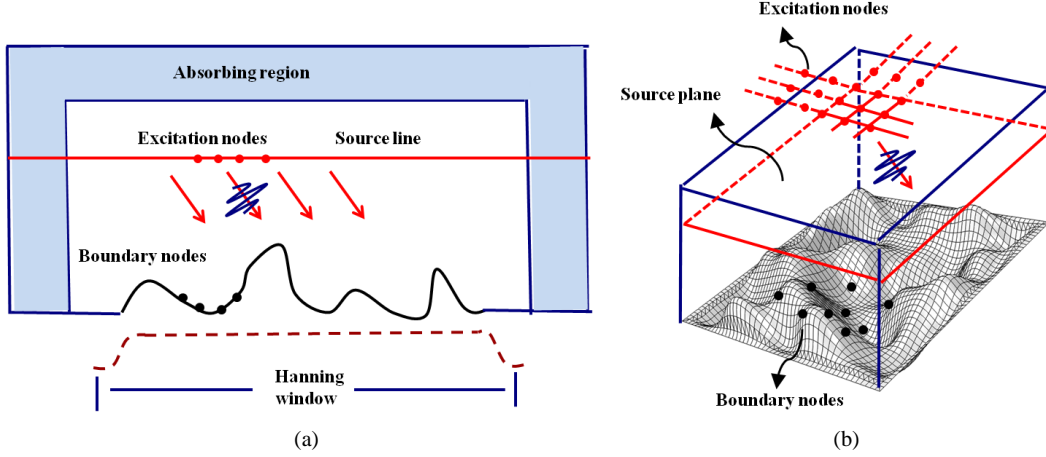


Figure 3. Sketches of the finite element boundary integration model to calculate the scattering waves from a rough backwall. (a) 2D model. (b) 3D model.

to calculate the scattered waves:

$$u_k^{sc}(\mathbf{R}) = \int_S \Sigma_{ijk}(|\mathbf{R} - \mathbf{r}|) u_i(\mathbf{r}) n_j(\mathbf{r}) dS(\mathbf{r}) \quad (2.5)$$

where Σ_{ijk} is the stress Greens tensor, u_i is the i th component of the total displacement, n_j is the j th component of the unit normal vector surface pointing towards the observation point at \mathbf{R} , and \mathbf{r} represents the position of the surface point.

With a far field approximation, Eq. (2.5) can be simplified as:

$$\mathbf{u}^{sc}(\mathbf{R}) = -ik_p \int_S \frac{e^{(ik_p D)}}{4\pi D} \mathbf{U}^p(\mathbf{r}, \mathbf{D}) dS(\mathbf{r}) - ik_s \int_S \frac{e^{(ik_s D)}}{4\pi D} \mathbf{U}^s(\mathbf{r}, \mathbf{D}) dS(\mathbf{r}). \quad (2.6)$$

Here

$$\begin{aligned} \mathbf{U}^p(\mathbf{r}, \mathbf{D}) &= \left[(\mathbf{u} \cdot \mathbf{n}) \left(1 - \frac{2k_p^2}{k_s^2} \right) + \frac{2k_p^2}{k_s^2} (\mathbf{u} \cdot \hat{\mathbf{D}})(\mathbf{n} \cdot \hat{\mathbf{D}}) \right] \hat{\mathbf{D}} \\ \mathbf{U}^s(\mathbf{r}, \mathbf{D}) &= (\mathbf{n} \cdot \hat{\mathbf{D}})\mathbf{u} + (\mathbf{u} \cdot \hat{\mathbf{D}})\mathbf{n} - 2(\mathbf{u} \cdot \hat{\mathbf{D}})(\mathbf{n} \cdot \hat{\mathbf{D}})\hat{\mathbf{D}} \end{aligned} \quad (2.7)$$

Before using the boundary displacements in Eq. (2.6), the Hanning window function is applied to them, to reduce the 'edge effects' in the approximation of an infinite surface. In 2D a popular way to approximate plane wave scattering from a truncation to an infinite surface is to use a tapered plane wave [21]. In this approximation the half beam width must be much smaller than the surface length, but roughly larger than 3λ to eliminate the tip effects. Unfortunately in 3D it is difficult to satisfy both criteria simultaneously due to the limited size of the 3D surface that can be simulated. Our approach is to apply a Hanning window to smooth the boundary displacement and, although this does not completely cancel the circular-crested waves from the edges, it does mitigate the effect substantially.

In practice Eq. (2.6) is implemented in the frequency domain and the results are synthesized back to the time domain to obtain the scattering signals using the inverse Fast Fourier Transform (IFFT). The model is extended to 3D by replacing the FE rectangular box with a cubic box, the 2D surface with a 3D surface and a source line with a source plane, as shown in Fig. (3)(b). Note that, for brevity, the absorbing region in 3D is not drawn here.

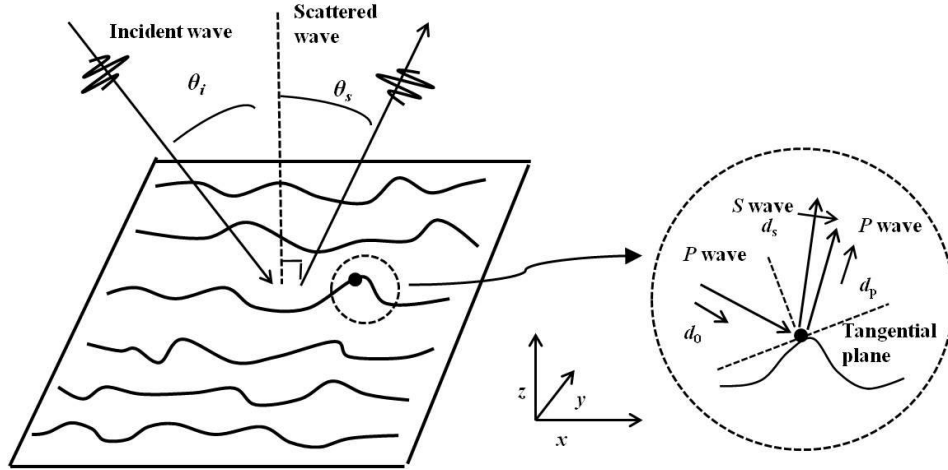


Figure 4. Sketch of the Kirchhoff model and the local view of the Kirchhoff approximation at one surface point.

(c) Elastic Kirchhoff model

The Kirchhoff model with a rough surface in the x - y plane is illustrated in Fig. (4). The KA assumes that the motion of a point on the surface is the same as if the point were part of an infinite plane insonified by the incident wave, as depicted in the zoom-in of Fig. (4). The total displacement at this point is calculated as a summation of the incident wave and the reflected compressional(P) and shear(S) waves:

$$\mathbf{u}_t = u_0(\mathbf{d}_0 + A_{pp}\mathbf{d}_p + A_{ps}\mathbf{d}_s). \quad (2.8)$$

Here \mathbf{u}_t represents the total displacement, u_0 is the amplitude of the incident P wave, A_{pp} and A_{ps} are reflection coefficients of P and S waves respectively and \mathbf{d}_0 , \mathbf{d}_p and \mathbf{d}_s are the displacement polarization vectors for the incident P and reflected P/S waves. The same Hanning window as implemented in the FE method is also applied to smooth the total displacement from KA to guarantee a fair comparison. By substituting the total displacement into Eq. (2.6), the scattering displacement is computed explicitly in the far field.

3. SIMULATIONS IN 2D AND 3D

In this paper, although we mainly investigate the compressional wave incidence/scattering case the method can also equally be applied to study shear wave scattering. For the simulations shown we use the material in the bulk medium to be Aluminium with Young's modulus of 70GPa, density of 2700kg/m³ and Poisson's ratio of 0.33. Thus the compressional wave speed is 6198m/s, and the shear wave speed is 3122m/s. The surfaces used follow the Gaussian distribution, which is generated by the moving average method discussed in Section 2. In 2D, 15 different rough surface profiles are tested with RMS $\sigma = \lambda_p/8, \lambda_p/6, \lambda_p/5, \lambda_p/4$ and $\lambda_p/3$, and correlation length $\lambda_0 = \lambda_p/2, \lambda_p/3$ and $\lambda_p/4$. While in 3D, 10 rough surface profiles are used with the same RMS values as those of the 2D cases, and with correlation lengths $\lambda_0 = \lambda_p/2$ and $\lambda_p/3$. In the 3D case the example with $\lambda_0 = \lambda_p/4$ is not used because this is too demanding for the 3D free-meshing algorithm which tends to fail when such a small correlation length is tested, and it should be noted that despite the efficiencies of the methodology, these calculations remain extremely demanding

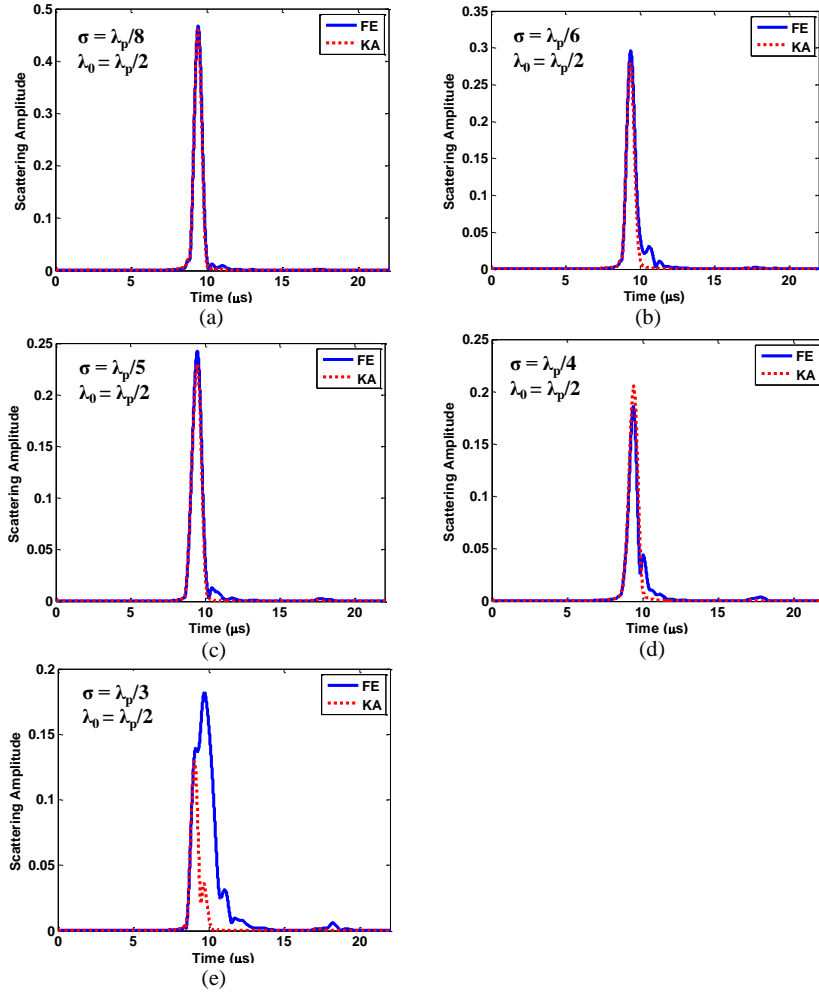


Figure 5. Hilbert transformed normal pulse echo scattering signals from one realization of surfaces with different roughness. (a) $\sigma = \lambda_p/8$, $\lambda_0 = \lambda_p/2$. (b) $\sigma = \lambda_p/6$, $\lambda_0 = \lambda_p/2$. (c) $\sigma = \lambda_p/5$, $\lambda_0 = \lambda_p/2$. (d) $\sigma = \lambda_p/4$, $\lambda_0 = \lambda_p/2$. (e) $\sigma = \lambda_p/3$, $\lambda_0 = \lambda_p/2$.

in terms of computer resources. Numerous simulations are run with incidence angles θ_i ranging from 0° to 30° to calculate scattering signals with θ_s from -90° to 90° . The distance from the surface to the far field projection point is 50mm ($\approx 32\lambda_p$). For each roughness, 50 realizations of surfaces are generated and Monte Carlo simulations are performed to obtain a statistically meaningful result for comparison between the KA and the FE method. The number of realizations is chosen by considering the conflicting requirements of both the statistical stability and the computational cost, especially in 3D. In NDT inspection scenarios we utilise the amplitude of the scattering signal because the amplitude directly determines the probability of detection [22]. The statistical parameter used for comparison is therefore the ensemble average of the peak of the Hilbert transformed scattered signals.

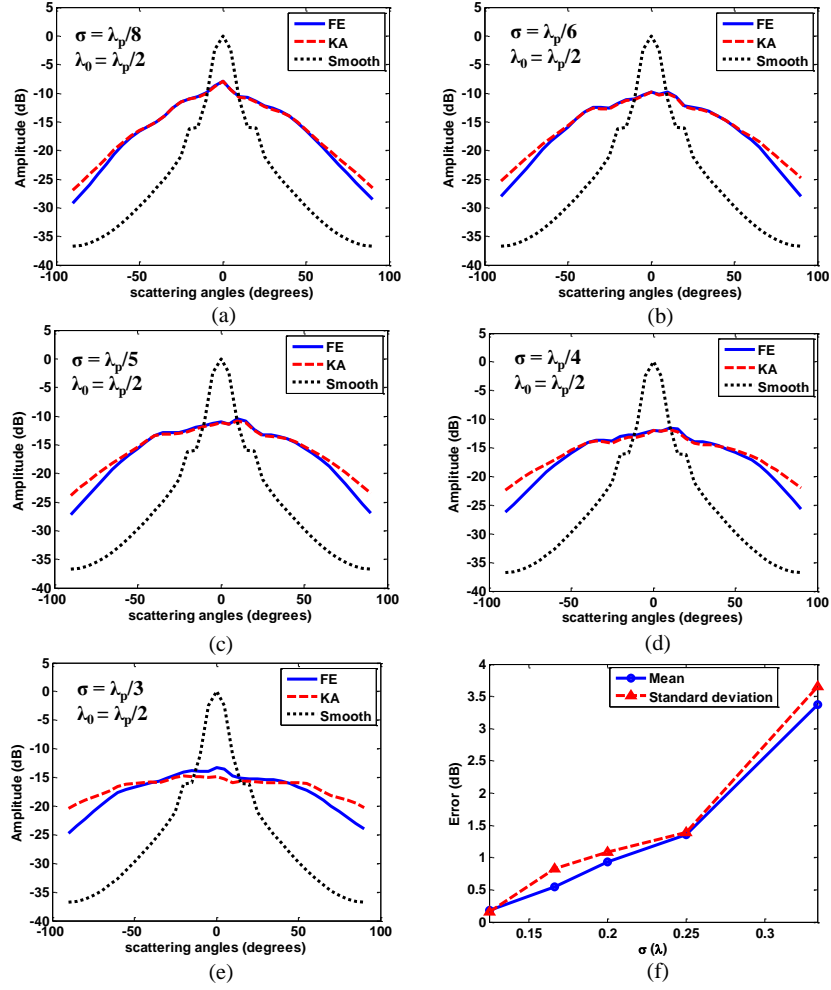


Figure 6. Comparison of the averaged peak amplitude of the scattering signals from 50 realizations between 2D FE and KA when $\theta_i = 0^\circ$. (a) $\sigma = \lambda_p/8$, $\lambda_0 = \lambda_p/2$. (b) $\sigma = \lambda_p/6$, $\lambda_0 = \lambda_p/2$. (c) $\sigma = \lambda_p/5$, $\lambda_0 = \lambda_p/2$. (d) $\sigma = \lambda_p/4$, $\lambda_0 = \lambda_p/2$. (e) $\sigma = \lambda_p/3$, $\lambda_0 = \lambda_p/2$. (f) Mean value and the standard deviation of the error when $\theta_i = \theta_s = 0^\circ$.

(a) Simulations using 2D rough surfaces

Simulations are first run using 2D surfaces and the corresponding FE model is meshed by linear triangular elements (equivalent to CPE3 in Abaqus (Dassault Systemes Simulia Corp., Providence, RI)) with an element size of $\lambda_p/30$. From earlier studies [23] this element size is sufficient for the convergence requirement in this study. With a proper partition, only the region surrounding the rough backwall is free meshed and the remaining region can be regularly meshed. A five-cycle Hanning windowed compressional wave with center frequency of 4MHz is used and the length of the 2D rough surface is about $5.2\lambda_p$. The dimension of the FE domain including the absorbing region is $14.8 \times 9.4 \text{ mm}^2 \approx 9.6\lambda_p \times 6.1\lambda_p$, and the thickness of the absorbing layers is 2.4mm ($\approx 1.5\lambda_p$).

For each scattering angle the compressional displacement is decomposed from the total displacement by using $\mathbf{u}_p = \mathbf{u}_x \sin(\theta_s) + \mathbf{u}_z \cos(\theta_s)$. Fig. (5) shows a set of plots of Hilbert transformed time traces of scattering signals from one realization of surfaces when $\theta_i = \theta_s = 0^\circ$,

with increased RMS values and a fixed correlation length. The amplitude is shown on a linear scale, and it is divided by the peak of the normal pulse echo response from a smooth surface of the same size. From Fig. (5), with a positive increment of the roughness, the amplitude of the scattering waves decreases significantly. In addition, the scattering waveforms become more complicated and a clear second arrival can be seen around $17\mu\text{s}$. This second arrival is the mode converted shear wave because it matches the correct arrival time, which equals to $4\text{mm}/(6198\text{m/s}) + 50\text{mm}/(3122\text{m/s}) = 16.7\mu\text{s}$. As shown in Fig. (5)(a) to (d), the Hilbert transformed scattering signals calculated from KA agree well with those from the FE method, when σ is smaller than $\lambda_p/4$. Such good agreement can no longer be seen in Fig. (5)(e), as the roughness increases to $\sigma = \lambda_p/3$, indicating that KA then becomes inaccurate.

Taking the mean value of the peak of these time traces from all realizations, the error between the KA and the FE across all scattering angles can be more accurately demonstrated by comparing the scattering patterns as in Fig. (6). For comparison the scattering pattern from a smooth surface with the same dimension is also shown. Only one curve is seen because the KA and the FE predict the same result for a smooth surface. Note that the angular spread is caused by both the finite length of the crack and the presence of the roughness. The amplitude is shown on the dB scale, and the reference is again the peak of the normal pulse echo response from a smooth surface. If more realizations are run we would expect the graph to become symmetric about $\theta_s = 0^\circ$. If the tolerance of error is set to be 1dB, as commonly used in NDE, the range of the scattering angle θ_s for which KA is acceptable is from -70° to 70° when $\sigma \leq \lambda_p/4$. However, if the RMS σ increases to $\lambda_p/3$ then, even at the specular direction the KA no longer matches with the FE. In addition, at near specular directions the KA underestimates the amplitude but at near grazing angles it overestimates the amplitude compared with the FE results; this is because multiple scattering phenomena are neglected in the KA. The consequences of neglecting the multiple scattering is that less energy is reflected back to the normal, or near normal, scattering angles and more energy than expected is distributed at near grazing angles. Fig. (6) (f) shows that both the mean absolute value and the standard deviation of the error at the normal backscattering direction increase as σ increases. The mean absolute error and the standard deviation are calculated using the following equations:

$$\begin{aligned}\bar{E} &= \frac{1}{N} \sum_{n=1}^N E_n = \frac{1}{N} \sum_{n=1}^N |A_n^{KA} - A_n^{FE}| \\ \text{std}(E) &= \sqrt{\frac{1}{N} \sum_{n=1}^N (E_n - \bar{E})^2}\end{aligned}\tag{3.1}$$

Here \bar{E} is the mean absolute error, E_n is the error for one realization, and N is the number of total realizations. A_n^{KA} and A_n^{FE} are the scattering amplitudes calculated from KA and FE for one realization respectively. $\text{std}(E)$ is the standard deviation of the error.

(b) Simulations using 3D rough surfaces

The 2D simulation results shown above are equivalent to 3D models using corrugated surfaces which have a height variation only in the x direction. Such simplifications have been performed in the past to ease computational demands [1,8,12], but in reality all defects have roughness in two dimensions. Although the range of validity for the 3D KA might, intuitively, not differ from the 2D KA much, some discrepancy between the two is expected given we now have roughness in one more direction.

The FE model as discussed and implemented with a 2D surface is extended to three dimensions with minor modifications. The 3D CAD software Rhino (Robert McNeel & Associates, Seattle, WA) was implemented to build the rough surfaces as shown for example in Fig. (7). The dimension of the rough surface is $5 \times 5\text{mm}^2$, that is approximately $3.3\lambda_p \times 3.3\lambda_p$. The surface is created by spline interpolating the surface point cloud generated using the moving average method. Restrictions are included in the interpolation algorithm so that the CAD surface is exactly

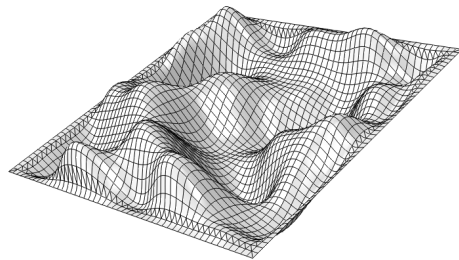


Figure 7. Sketch of a typical rough surface with $\sigma = \lambda/3$, $\lambda_0 = \lambda/2$.

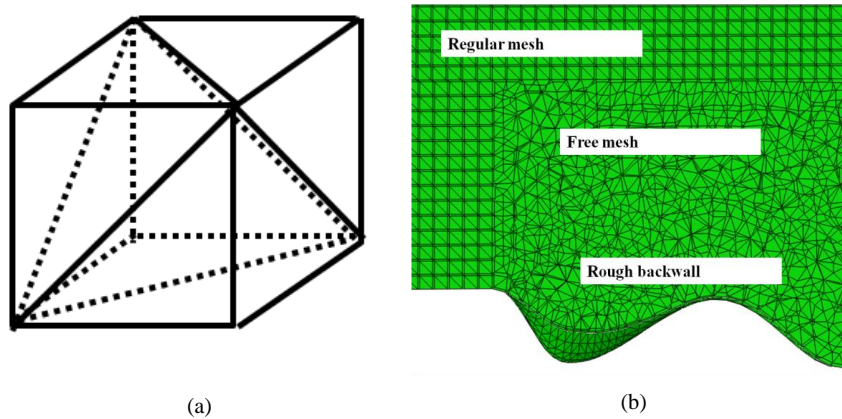


Figure 8. Mesh profile in 3D. (a) One cell composed of six tetrahedron elements. (b) Local view of the 3D mesh.

on the positions of the generated points. This is crucial to guarantee that the produced surface does not deviate from the required point position, and consequently to avoid any smoothing effect caused by general surface interpolation algorithms.

Free meshing algorithms using linear tetrahedral elements (C3D4 in Abaqus) are commonly utilized for the 3D FE modelling of scattering from obstacles with irregular geometries [24,25]. As is well known, free meshing tends to randomize the distribution and the shape of each element, and thus may introduce unwanted mesh-scattering and dispersion [26]. We therefore combine two different meshing algorithms in 3D with a code developed using Matlab (MathWorks, Natick, MA). The region just above the 3D rough surface is meshed via a free meshing algorithm to produce elements around the surfaces. This very local meshing profile is then used as an input to the code to grow a regular mesh to fill up the remaining region of the 3D model. The regular meshed region is meshed with many hexahedral cells and each cell is composed of six linear tetrahedral elements as shown in Fig. (8)(a). The dimension of the 3D FE domain including

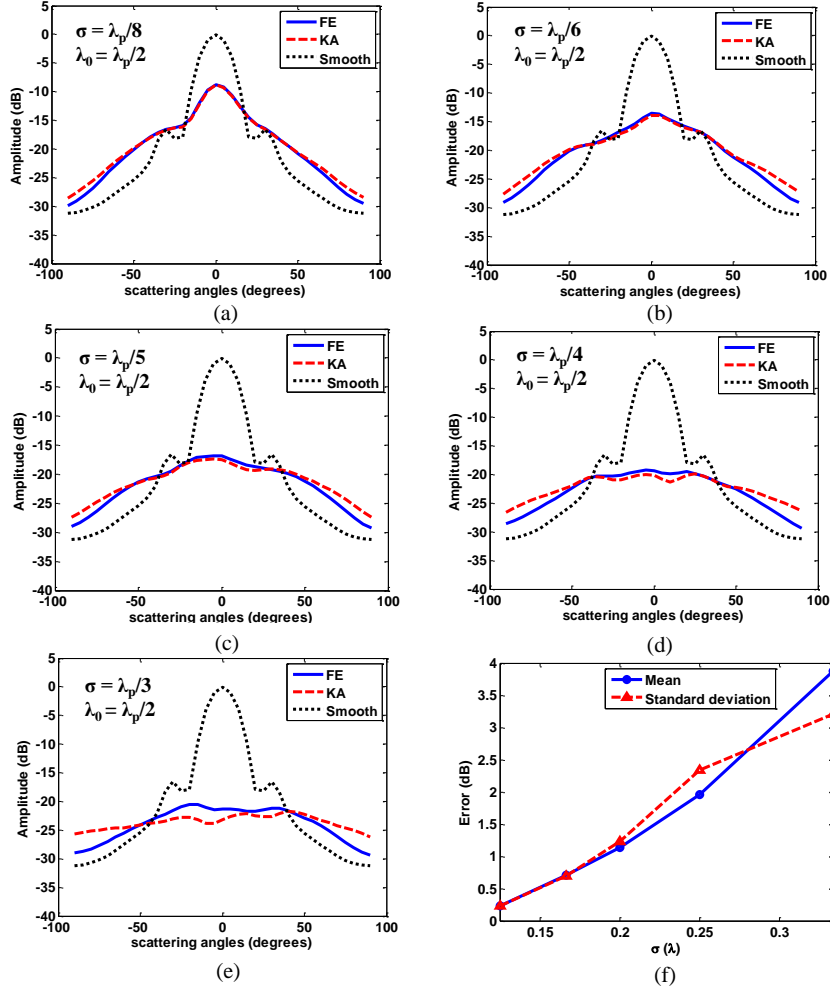


Figure 9. Comparison of the averaged peak amplitude of the scattering signals from 50 realizations between 3D FE and KA when $\theta_i = 0^\circ$. (a) $\sigma = \lambda_p/8$, $\lambda_0 = \lambda_p/2$. (b) $\sigma = \lambda_p/6$, $\lambda_0 = \lambda_p/2$. (c) $\sigma = \lambda_p/5$, $\lambda_0 = \lambda_p/2$. (d) $\sigma = \lambda_p/4$, $\lambda_0 = \lambda_p/2$. (e) $\sigma = \lambda_p/3$, $\lambda_0 = \lambda_p/2$. (f) Mean value and the standard deviation of the error when $\theta_i = \theta_s = 0^\circ$.

the absorbing region is $12.8 \times 12.8 \times 4.4 \text{mm}^3$ ($\approx 8.3\lambda_p \times 8.3\lambda_p \times 2.9\lambda_p$), and the thickness of the absorbing layers is 2.4mm ($\approx 1.5\lambda$).

Fig. (8)(b) shows a local view of the mesh profile of one 3D FE model. It should be noted that at the boundary of the free meshing and the regular meshing regions, the two neighboring elements need to have the same hypotenuse to prevent any spurious reflection. In this manner, the mesh minimizes the complexity caused by the free meshing algorithm whilst still capturing the exact shape of the complex rough surface.

In a similar manner to that deployed in the 2D studies a Monte Carlo simulation is performed, with various roughness and incidence/scattering angles, and the averaged peak amplitudes from 50 realizations are compared between the KA and the FE model. Fig. (9) shows the comparison for the case of a normally incident wave. Good agreement can be seen from -70° to 70° when $\sigma = \lambda_p/8$, $\lambda_p/6$, $\lambda_p/5$ and $\lambda_p/4$. The scattering pattern from a smooth surface with the same dimension is also shown for comparison. However, when σ increases to $\lambda_p/3$, the agreement no longer exists even in the normal backscattering direction. Note that the errors

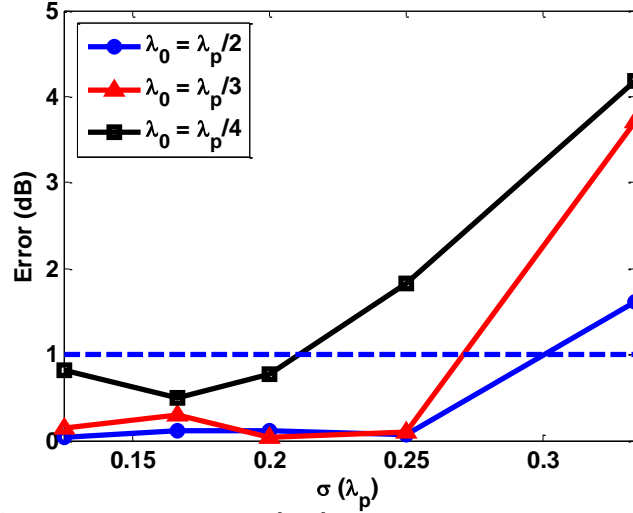


Figure 10. Error of the averaged peak amplitude ($\theta_i = \theta_s = 0^\circ$) between 2D FE and KA with respect to σ when $\lambda_0 = \lambda_p/2$, $\lambda_p/3$ and $\lambda_p/4$.

between the KA and the FE are relatively higher than the corresponding 2D cases in Fig. (6). Again the mean absolute error and the corresponding standard deviation for each σ are plotted in Fig. (9)(f).

4. ERROR ANALYSIS IN 2D AND 3D

(a) The effect of surface roughness

As mentioned by Ogilvy [7], historically the most frequently cited validity criterion from a geometrical point of view for the KA is $kr_c \cos^3 \theta_i \gg 1$, in which r_c is the local radius of curvature and θ_i is the global angle of incidence. This equation explains the fundamental restriction of the rate of change of the surface height gradient, which determines the validity of the tangential plane assumption used as a starting point for the KA. However, other related works [1,10] indicate that this commonly used criterion has not proved to be practically useful. The errors from the KA are not only from the 'local' geometrical tangential plane assumption, but also arise from 'global' effects, such as multiple scattering and shadowing effects due to the overall shape of the rough surface. These 'global' errors become larger as the roughness or the frequency increases, and the corresponding 'global' effects are not easy to quantify directly. Thorsos [1] suggests the use of λ_0 as a crucial surface parameter including both the local and the global effects. In this section we propose a different surface parameter for elastic materials, a function of both λ_0 and σ to give a rough idea when the use of the KA is valid for practical applications.

Figure (10) shows the errors of the averaged peak amplitude between the 2D KA and the FE with respect to the RMS σ , with a normal incident/backscattering configuration. Different curves represent the numerical errors using surfaces with different correlation lengths. The tolerance of error is set to the value commonly used in NDE applications of 1dB, as shown by the flat dashed line, indicating that the roughness is acceptable for the use of KA once the corresponding error is below this threshold. The maximum values of σ for a given correlation length λ_0 and

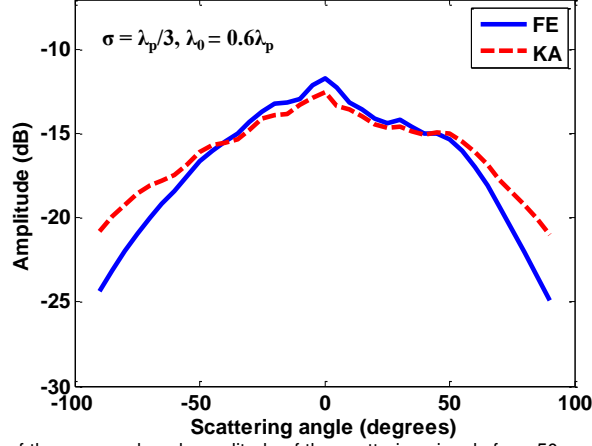


Figure 11. Comparison of the averaged peak amplitude of the scattering signals from 50 realizations ($\theta_i = 0^\circ$) between 2D FE and KA, when $\sigma = \lambda_p/3$, $\lambda_0 = 0.6\lambda_p$.

error tolerance can hence be found by observing the trend of the error curves. These values are summarized in Table 1.

Clearly, as can be seen from Fig. (10), increasing the RMS σ and decreasing the correlation length λ_0 result in a larger value of the error. This increase in error is because the surface effectively becomes more rough when changing the two surface parameters in this manner. Therefore we propose a simple criterion as a function of both σ and λ_0 , based on the inversely proportional relationship:

$$\frac{\sigma^a}{\lambda_0} \leq c \quad (4.1)$$

where a is the weighting factor for σ and c is an unknown constant representing an upper bound for this inequality. Note that this form is not unique, for example one may also assume a weighting factor for λ_0 instead of σ . However, in this paper we propose Eq. (4.1) and it will be shown later that this formulation can approximately estimate the region of validity of the KA in both 2D and 3D.

The acceptable values of σ and λ_0 can be explicitly calculated from this formula once a and c are known. An alternative form converted from Eq. (4.1) is used here to estimate these two unknown coefficients.

$$\frac{\sigma_{\max}^a}{\lambda_0} = c \quad (4.2)$$

Substituting the three values of $\sigma_{\max 2D}$ from Table. 1 into Eq. (4.2) and taking the log of both sides yields the following form of matrix multiplication:

$$\begin{pmatrix} \log_{10} \sigma_{\max 1} & -1 \\ \log_{10} \sigma_{\max 2} & -1 \\ \log_{10} \sigma_{\max 3} & -1 \end{pmatrix} \begin{pmatrix} a \\ \log_{10} c \end{pmatrix} = \begin{pmatrix} \log_{10} \lambda_{01} \\ \log_{10} \lambda_{02} \\ \log_{10} \lambda_{03} \end{pmatrix} \quad (4.3)$$

By multiplying the term on the righthand side with the pseudo inverse of the first term on the left side, the weighting factor a and the upper bound c are calculated in the sense of least

squares. Recalling that we are using the tolerance of 1dB, typical of NDE, from the calculation we see that for this error $a \approx 2$. The value of a could change if a more or less stringent tolerance of error were required. The observed criterion for the validity of KA can be expressed as:

$$\frac{\sigma^2}{\lambda_0} \leq 0.2\lambda_p \quad (4.4)$$

This criterion can be applied to find the σ_{\max} with a given λ_0 or the $\lambda_{0\min}$ with a given σ :

$$\sigma_{\max} = (0.2\lambda_p \times \lambda_0)^{\frac{1}{2}} \quad \text{and} \quad \lambda_{0\min} = \frac{\sigma^2}{0.2\lambda_p} \quad (4.5)$$

A numerical case is performed here to test the proposed criterion. As can be seen from Fig. (10), when $\sigma = \lambda_p/3$ the errors for all curves are above the 1dB threshold, which implies that the acceptable λ_0 needs to be larger than $\lambda_p/2$. By substituting $\sigma = \lambda_p/3$ into Eq. (4.5), $\lambda_{0\min}$ is estimated to be roughly $0.6\lambda_p$. A Monte Carlo simulation with 50 surfaces is run for this specific σ and λ_0 , as was performed with the other roughness tested. As can be seen from Fig. (11), the error between the KA and the FE method when $\theta_i = \theta_s = 0^\circ$ is 0.86dB. This error is just below the 1dB threshold, implying that when $\sigma = \lambda_p/3$, $\lambda_{0\min} = 0.6\lambda_p$, which is the same as the value predicted from Eq. (4.5). The simple empirical criterion proposed from observation can therefore be applied to roughly estimate the region of validity of KA.

(b) The effect of scattering/incidence angle

The Kirchhoff theory is known to be insufficient to model the scattering of waves at large scattering angles [7]. For example as seen from Fig. (6)(a) to (d), the scattering amplitude calculated by the KA is several dB higher than the FE when the scattering angle $\theta_s > 70^\circ$. The explanation given in section 3 is that the KA cannot account for multiple scattering effects.

In the same way large incidence angles also result in considerable errors of the Kirchhoff model. In this study, we alternatively focus on the effect of modest incidence angles on the accuracy of the KA. Specifically, we compared the averaged scattering amplitude of the KA and the FE at incidence angles from 0° to 30° with an interval of 5° . Fig. (12)(a) shows the comparison results of the amplitude with a slightly oblique incidence angle ($\theta_i = 30^\circ$) when $\sigma = \lambda_p/3$, $\lambda_0 = \lambda_p/2$. Excellent agreement is found with the scattering angle θ_s ranging from -65° to 65° . It is different from the case with the normal incidence angle as shown in Fig. (6)(e), where the error is above 1dB. It indicates that even with a very rough crack, an acceptable inspection result may still be achieved using the Kirchhoff model with a small oblique incidence angle. Fig. (12)(b) further illustrates this point as the error of the scattering signal at the specular direction is plotted as a function of the incidence angle. As can be clearly seen, the error decays as the incidence angle increases for the curve representing $\sigma = \lambda_p/3$; for the other curves when $\sigma < \lambda_p/3$, the error roughly remains the same, well within 1dB. The results for surfaces with a correlation length of $\lambda_p/2$ are shown here but the trend is typical for all other correlation lengths tested in this paper.

The 'Rayleigh parameter' [7] which has been used to classify the rough surface and the smooth surface can be quoted here to give a qualitative physical explanation. The Rayleigh parameter is

$$R_a = k\sigma \cos \theta_i \quad (4.6)$$

which represents statistically the relative phase difference between the reflected waves from two random surface points observed in the specular direction. The larger the value of R_a , the more destructively the two reflected waves interfere with each other. Therefore it is one feature which is proportional to the roughness of the surface. According to Eq. (4.6), if the Rayleigh parameter R_a is fixed then the RMS σ is inversely a measure of $\cos \theta_i$. This suggests that for a fixed R_a , with a modest incidence angle the maximum value of σ can be relatively larger than that when $\theta_i = 0^\circ$. It should be noted that the effect of a modest incident angle is qualitatively analyzed here by the use of the Rayleigh parameter, but it cannot be applied in the same manner when the incidence angle is large.

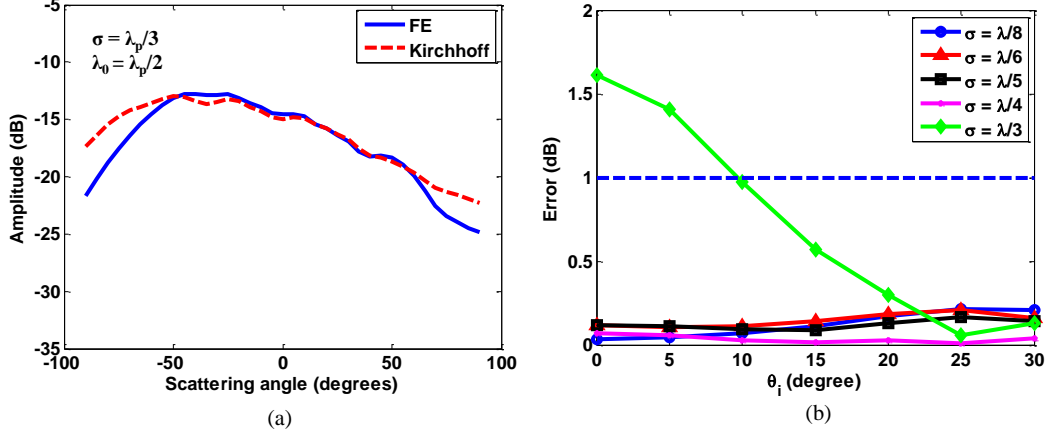


Figure 12. Effects of a modest incidence angle on the accuracy of KA in 2D. (a) Comparison of the averaged peak amplitude from 50 realizations ($\theta_i = 30^\circ$) between 2D FE and KA when $\sigma = \lambda_p/3$, $\lambda_0 = \lambda_p/2$. (b) Error of the averaged peak amplitude between 2D FE and KA with respect to θ_i in the specular direction when $\sigma = \lambda_p/8$, $\lambda_p/6$, $\lambda_p/5$, $\lambda_p/4$, $\lambda_p/3$, and $\lambda_0 = \lambda_p/2$.

λ_0	$\lambda_p/2$	$\lambda_p/3$	$\lambda_p/4$
$\sigma_{\max 2D}$	$0.31\lambda_p$	$0.27\lambda_p$	$0.22\lambda_p$
$\sigma_{\max 3D}$	$0.27\lambda_p$	$0.22\lambda_p$	—

Table 1. Maximum values of σ for a known λ_0 with 1dB error of tolerance estimated from Fig. (10) (2D) and Fig. (13) (3D).

(c) The effect of dimension (2D or 3D)

Similar criteria for the 3D KA can be proposed in the same manner as was deployed for 2D. Fig. (13) shows the error between the KA and the FE method with respect to σ for two different values of λ_0 . Similar trends can be observed in the two curves but the errors are relatively higher, compared with those in Fig. (10) for the 2D KA. The same strategy is implemented to estimate the unknown parameters in Eq. (4.2), but using $\sigma_{\max 3D}$ from Table 1. By using the least squares method, the best fitted weighting factor remains at $a \approx 2$, and the upper bound reduces to $c = 0.14\lambda_p$. The criterion in 3D can therefore be expressed as:

$$\frac{\sigma_{\max}^2}{\lambda_0} \leq 0.14\lambda_p \quad (4.7)$$

It is notable that the upper bound $0.14\lambda_p$ is smaller than the corresponding value $0.2\lambda_p$ in 2D, which highlights one important discrepancy of the validity between the KA in 2D and 3D. Specifically, as we can see, the values of σ_{\max} for a given λ_0 in 3D are smaller than those in 2D as shown in Table 1; this implies that the criterion for the 3D KA is stricter than that in 2D. We can consider this by examining the surface locally, where we know that the magnitude of the gradient of one surface point in 2D and 3D can be expressed as

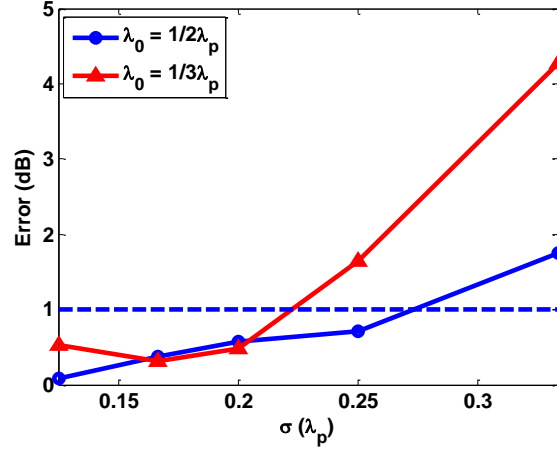


Figure 13. Error of the averaged peak amplitude between 3D FE and KA ($\theta_i = \theta_s = 0^\circ$) with respect to σ when $\lambda_0 = \lambda_p/2$ and $\lambda_p/3$.

$$|\nabla h(x)|_{2D} = \left| \frac{\partial h}{\partial x} \right|_{2D} \quad \text{and,} \quad |\nabla h(x, y)|_{3D} = \sqrt{\left| \frac{\partial h}{\partial x} \right|_{3D}^2 + \left| \frac{\partial h}{\partial y} \right|_{3D}^2}. \quad (4.8)$$

Obviously from the above equation, $|\nabla h(x, y)|_{3D}$ is larger than $|\nabla h(x)|_{2D}$ if it is assumed that $\left| \frac{\partial h}{\partial x} \right|_{2D} = \left| \frac{\partial h}{\partial x} \right|_{3D}$, which is due to adding an additional term $\left| \frac{\partial h}{\partial y} \right|_{3D}$. The conclusion is that the rate of change of height is faster for the 3D surface which consequently appears rougher than the corresponding 2D surface.

Apart from this, height variations in the y direction can contribute to out of plane scattering effects besides the scattering waves inside the x - z plane. Globally more shadowing effects and multiple scattering would occur, due to the roughness in the extra dimension. It would result in extra errors of the 3D KA in addition to the local errors from the tangential plane assumption. As a result, restrictions on the validity of 3D KA are made more severe than the 2D KA due to this one more dimension of roughness.

If the incidence angle is slightly oblique at 30° , as in Fig. (14)(a), then the FE and the KA models show agreement, but only within a very narrow angular range around the specular direction, roughly from 30° to 50° . In contrast, the acceptable region of the scattering angles in 2D with the same roughness is much larger, ranging from -65° to 65° , as shown in Fig. (12)(a). This rapidly reduced angular range in 3D when $\sigma = \lambda_p/3$ is another important feature between the region of validity of 3D and 2D KA. It may be because in 3D there are more multiple scattering and mode conversions than 2D, which are not modelled using the KA. The scattering waves contributed from these phenomena would spread to all scattering angles, reducing the accuracy of the 3D KA at non-specular directions. On the other hand, the effect of a modest incidence angle on the 3D KA is demonstrated in Fig. (14)(b). All the curves representing different σ show a decay of the error when increasing the incidence angle θ_i . The errors are relatively higher than those shown in Fig. (12)(b) for the 2D cases.

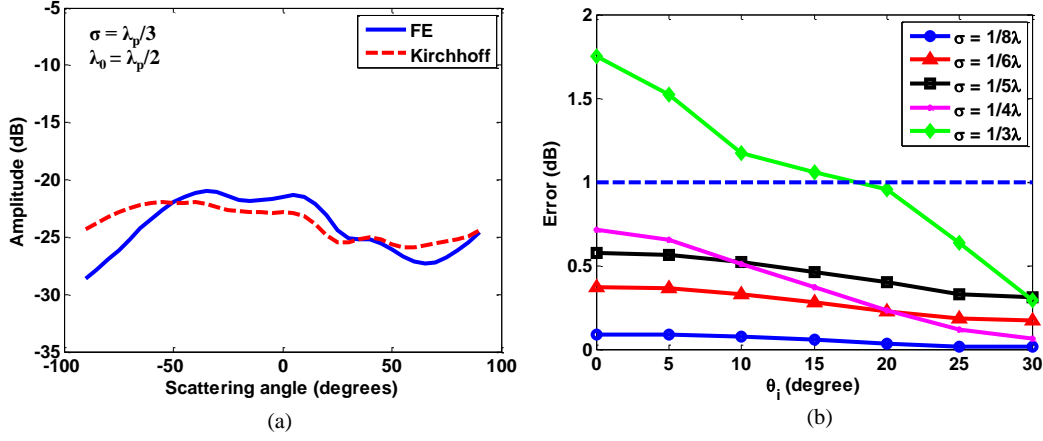


Figure 14. Effects of a modest incidence angle on the accuracy of KA in 3D. (a) Comparison of the averaged peak amplitude from 50 realizations ($\theta_i = 30^\circ$) between 3D FE and KA when $\sigma = \lambda_p/3$, $\lambda_0 = \lambda_p/2$. (b) Error of the averaged peak amplitude between 3D FE and KA with respect to θ_i in the specular direction when $\sigma = \lambda_p/8$, $\lambda_p/6$, $\lambda_p/5$, $\lambda_p/4$, $\lambda_p/3$, and $\lambda_0 = \lambda_p/2$.

5. CONCLUSIONS

A numerical study to determine the range of validity of the Kirchhoff approximation as used to calculate the elastic wave scattering signals from Gaussian rough surfaces has been performed. The Kirchhoff theory is evaluated for comparison with a FE method using 2D and 3D isotropic surfaces with different roughness characterized by RMS σ and correlation length λ_0 . Monte Carlo simulations of multiple realizations are run with a variety of incidence/scattering angles, and the averaged peak amplitude of the scattering signals are used for comparison. It is found that, with a normal incidence angle $\theta_i = 0^\circ$, the KA is valid when $\sigma^2/\lambda_0 \leq c$, with $-70^\circ < \theta_s < 70^\circ$. In addition, a modest incidence angle within 30° can improve the accuracy of the KA when σ^2/λ_0 exceeds the constant upper bound c . The above criteria are derived empirically for an estimation of the region of validity of the KA.

We have particularly examined the difference of the valid region with 2D and 3D surfaces and have found that the criterion for the 3D KA is stricter. First of all when $\theta_i = 0^\circ$, the upper bound c of σ^2/λ_0 in 2D is $0.20\lambda_p$, and in 3D it reduced to $0.14\lambda_p$. In other words, the acceptable range of σ and λ_0 in 3D is smaller than those in 2D, which is the most important discrepancy between the 2D and 3D KA. This is caused by the increased local RMS gradient, and the global multiple reflections and shadowing effects as well. Furthermore, similar to 2D, a modest incidence angle of less than 30° can also improve the accuracy of the 3D KA. However, the acceptable angular range of the scattering angle is dramatically reduced compared with the same situation in 2D, being only around the specular direction. In fact these differences arise from extra surface height variations in one more dimension, which makes 3D surfaces as viewed by the incident wave appear to be rougher. In practice, the criteria for the 3D KA must be taken into consideration in a real NDE inspection because naturally all real defects are rough in 3D.

6. Ethics statement

The paper does not include any contents regarding animals or human subjects.

7. Data accessibility

Data has been submitted as an attachment document.

8. Competing interests

We have no competing interests.

9. Authors' contribution

Contribution of F. Shi: Perform all simulations, analyze data and write the paper. Contributions of W. Choi, M. J. S. Lowe, E. A. Skelton and R. V. Craster: Provide valuable discussions with the first author and critically revise the paper.

Acknowledgment

The authors are grateful to the UK Research Centre in Non Destructive Evaluation (RCNDE), the Engineering and Physical Science Research Council (EPSRC), and to Amec Foster Wheeler, Rolls-Royce Marine and EDF Energy, for funding this work.

References

1. Thorsos EI. 1988 The validity of the Kirchhoff approximation for rough surface scattering using a Gaussian roughness spectrum, *J. Acoust. Soc. Am.* **83**, 78–92.
2. Berry MV. 1973 The statistical properties of echoes diffracted from rough surfaces, *Phil. Trans. R. Soc. Lond. A* **273**, 611–654.
3. Robertsson JOA, Laws R, Chapman C, Vilotte JP, Delavaud E. 2006 Modelling of scattering of seismic waves from a corrugated rough sea surface: a comparison of three methods, *Geophys. J. Int.* **167**, 70–76.
4. Laws R, Kragh E. 2002 Rough seas and time lapse seismic, *Geophys. Prospect.* **167**, 195–208.
5. Ogilvy JA. 1989 Model for the ultrasonic inspection of rough defects, *Ultrasonics* **27**, 69–79.
6. Zhang J, Drinkwater BW, Wilcox PD. 2012 Effect of roughness on imaging and sizing rough crack-like defects using ultrasonic arrays, *IEEE Trans. Ultrason. Ferroelectr. Freq. Control.* **59**, 939–948.
7. Ogilvy JA. 1991 *Theory of Wave Scattering from Random Rough Surfaces*, Adam Hilger Ltd.
8. Ogilvy JA. 1986 An estimate of the accuracy of the Kirchhoff approximation in acoustic wave scattering from rough surfaces, *J. Phys. D: Appl. Phys.* **19**, 2085–2113.
9. Thorsos EI. 1990 Acoustic scattering from a 'Pierson-Moskowitz' sea surface, *J. Acoust. Soc. Am.* **88**, 335–349.
10. Chen MF, Fung AK. 1988 A numerical study of the regions of validity of the Kirchhoff and small-perturbation rough surface scattering models, *Radio Science* **23**, 163–170.
11. Roberts RA. 2012 The effect of crack morphology on ultrasonic response, In *Review of Progress in Quantitative NDE* (eds. DO Thompson, DE Chimenti), *AIP Conference Proceedings*, volume 1430, 150–157. American Institute of Physics, Denver, CO.
12. Zhang J, Drinkwater BW, Wilcox PD. 2011 Longitudinal wave scattering from rough crack-like defects, *IEEE Trans. Ultrason. Ferroelectr. Freq. Control.* **58**, 2171–2180.
13. Shi F, Choi W, Skelton EA, Lowe MJS, Craster RV. 2014 A time domain finite element boundary integration method for ultrasonic non-destructive evaluation, *IEEE Trans. Ultrason. Ferroelectr. Freq. Control.* **61**, 2054–2066.
14. Velichko A, Wilcox PD. 2010 A generalized approach for efficient finite element modeling of elastodynamic scattering in two and three dimensions, *J. Acoust. Soc. Am.* **128**, 1004–1014.

15. Chapman RK, Pearce JE, Burch SF, Fradkin L, Toft MW. 2007 Recent in-house developments in theoretical modelling of ultrasonic inspection, *Insight* **49**, 93–97.
16. Ogilvy JA. 1988 Computer simulation of acoustic wave scattering from rough surfaces, *J. Phys. D: Appl. Phys.* **21**, 260–277.
17. Huthwaite P. 2014 Accelerated finite element elastodynamic simulations using the GPU, *J. Comput. Phys.* **257**, 687–707.
18. Pettit JR, Walker A, Cawley P, Lowe MJS. 2014 A stiffness reduction method for efficient absorbing of waves at boundaries for use in commercial Finite Element codes, *Ultrasonics* **54**, 1868–1879.
19. Skelton EA, Craster RV, Choi W, Lowe MJS. 2013 Numerical simulations of ultrasound NDE: A hybrid model with improved efficiency by a new boundary forcing method, In *Proceedings of the 10th International Conference on NDE in Relation to Structural Integrity for Nuclear and Pressurised Components*, 602–609.
20. Ogilvy JA, Culverwell ID. 1991 Elastic model for simulating ultrasonic inspection of smooth and rough defects, *Ultrasonics* **29**, 490–496.
21. Schultz CA, Toksoz MN. 1993 Enhanced backscattering of seismic waves from a highly irregular, random interface: Sh case, *Geophys. J. Int.* **114**, 91–102.
22. Pettit JR, Walker A, Lowe MJS. 2014 Improved detection of rough defects for ultrasonic nde inspections based on finite element modeling of elastic waves, In *Review of Progress in Quantitative NDE* (eds. DO Thompson, DE Chimenti), *AIP Conference Proceedings*, volume 1581, 521–528. American Institute of Physics, Boise, ID.
23. Drozd MB. 2008 Efficient finite element modelling of ultrasound waves in elastic media. Ph.D. thesis, Imperial College London.
24. Schaubert D, Wilton DR, Glisson AW. 1984 A tetrahedral modeling method for electromagnetic scattering by arbitrarily shaped inhomogeneous dielectric bodies, *IEEE Trans. Antennas. Propagation.* **32**, 77–85.
25. Lawrence H, Demontoux F, Wigner JP, Paillou P, Wu TD, Kerr YH. 2011 Evaluation of numerical modeling approach based on the finite-element method for calculating the rough surface scattering and emission of a soil layer, *IEEE Geosci. Remo. Sens. Lett.* **8**, 953–957.
26. Rajagopal P, Drozd MB, Lowe MJS. 2008 Towards improved finite element modelling of the interaction of elastic waves with complex defect geometries, In *Review of Progress in Quantitative NDE* (eds. DO Thompson, DE Chimenti), volume 28a, 49–56. American Institute of Physics, Chicago, IL.